



HAL
open science

Performance Evaluation and Compatibility Studies of a Compact Preclinical Scanner for Simultaneous PET/MR Imaging at 7 Tesla

Alan Courteau, John Mcgrath, Paul Michael Walker, Rosie Pegg, Gary Martin, Ruslan Garipov, Peter Doughty, Alexandre Cochet, Francois Brunotte, Jean-Marc Vrigneaud

► To cite this version:

Alan Courteau, John Mcgrath, Paul Michael Walker, Rosie Pegg, Gary Martin, et al.. Performance Evaluation and Compatibility Studies of a Compact Preclinical Scanner for Simultaneous PET/MR Imaging at 7 Tesla. IEEE Transactions on Medical Imaging, 2021, 40, pp.205 - 217. 10.1109/tmi.2020.3024722 . hal-03118426

HAL Id: hal-03118426

<https://u-bourgogne.hal.science/hal-03118426>

Submitted on 22 Jan 2021

HAL is a multi-disciplinary open access archive for the deposit and dissemination of scientific research documents, whether they are published or not. The documents may come from teaching and research institutions in France or abroad, or from public or private research centers.

L'archive ouverte pluridisciplinaire **HAL**, est destinée au dépôt et à la diffusion de documents scientifiques de niveau recherche, publiés ou non, émanant des établissements d'enseignement et de recherche français ou étrangers, des laboratoires publics ou privés.

Performance Evaluation and Compatibility Studies of a Compact Preclinical Scanner for Simultaneous PET/MR Imaging at 7 Tesla

Alan Courteau¹, John McGrath, Paul Michael Walker, Rosie Pegg, Gary Martin, Ruslan Garipov, Peter Doughty, Alexandre Cochet, François Brunotte, and Jean-Marc Vrigneaud

Abstract—We present the design and performance of a new compact preclinical system combining positron emission tomography (PET) and magnetic resonance imaging (MRI) for simultaneous scans. The PET contains sixteen SiPM-based detector heads arranged in two octagons and covers an axial field of view (FOV) of 102.5 mm. Depth of interaction effects and detector's temperature variations are compensated by the system. The PET is integrated in a dry magnet operating at 7 T. PET and MRI characteristics were assessed complying with international standards and interferences between both subsystems during simultaneous scans were addressed. For the rat size phantom, the peak noise equivalent count rates (NECR) were 96.4 kcps at 30.2 MBq and 132.3 kcps at 28.4 MBq respectively with and without RF coil. For mouse, the peak NECR was 300.0 kcps at 34.5 MBq and 426.9 kcps at 34.3 MBq respectively with and without coil. At the axial centre of the FOV, spatial resolutions expressed as full width at half maximum / full width at tenth maximum (FWHM/FWTM) ranged from 1.69/3.19 mm to 2.39/4.87 mm. The peak absolute sensitivity obtained with a 250-750 keV energy window was 7.5% with coil and 7.9%

without coil. Spill over ratios of the NEMA NU4-2008 image quality (NEMA-IQ) phantom ranged from 0.25 to 0.96 and the percentage of non-uniformity was 5.7%. The image count versus activity was linear up to 40 MBq. The principal magnetic field variation was 0.03 ppm/mm over 40 mm. The qualitative and quantitative aspects of data were preserved during simultaneous scans.

Index Terms—Magnetic resonance imaging, nuclear imaging, evaluation and performance, PET/MR interferences.

I. INTRODUCTION

POSITRON emission tomography (PET) coupled with Magnetic Resonance Imaging (MRI) offers many benefits to preclinical investigations as it combines the excellent spatial and temporal resolution of MRI with the high sensitivity of PET. The combination of PET with MRI provides a better and more flexible tissue discrimination than X-ray computed tomography without resorting to ionizing radiation [1], [2]. Besides morphological information, MRI can also bring complementary functional information such as tissue perfusion or metabolism. Hence, the interest in PET/MRI has been boosted in preclinical research as coupling PET and MRI dramatically increases the amount of physiological information that can be collected during a single anaesthesia. During the last decade, design and instrumentation of small animal PET/MR systems have drastically improved. Former approaches have been based on an in-line geometry either with avalanche photodiodes (APD) [2], [3] or more recently with silicon photomultipliers (SiPM) [4]. These in-line imaging systems allowed a sequential acquisition, thanks to an axial translation of the animal from one modality to the other.

More challenging simultaneous PET/MR scanners have also been developed. To our knowledge, four of these systems have been described in the literature, namely the MADPET4 [5], [6], the SimPET [7]–[9], the HYPERION-II [10]–[12], and the system described by Stortz *et al.* [13]–[15]. In these systems, the PET instrumentation is integrated inside the MR bore, with the field of view (FOV) of each modality overlapping. These scanners allow the acquisition of both modalities during a much shorter anaesthesia. Moreover, the animals are studied in exactly the same physiological condition,

Manuscript received May 27, 2020; revised July 31, 2020; accepted September 10, 2020. Date of publication September 21, 2020; date of current version December 29, 2020. This work was supported by the French National Research Agency under Grant ANR-10-EQPX-05-01. (Corresponding author: Alan Courteau.)

Alan Courteau and François Brunotte are with the Laboratoire Imagerie et Vision Artificielle, EA 7535, University of Bourgogne-Franche-Comté, 21000 Dijon, France (e-mail: alan.courteau@u-bourgogne.fr; francois.brunotte@u-bourgogne.fr).

John McGrath, Rosie Pegg, Gary Martin, Ruslan Garipov, and Peter Doughty are with MR Solutions Ltd., Guildford GU4 7WA, U.K. (e-mail: john.mcgrath@mrsolutions.com; rosie.pegg@mrsolutions.com; gary.martin@mrsolutions.com; ruslan.garipov@mrsolutions.com; peter.doughty@mrsolutions.com).

Paul Michael Walker is with the Laboratoire Imagerie et Vision Artificielle, EA 7535, University of Bourgogne-Franche-Comté, 21000 Dijon, France, and also with the CHU François Mitterrand, 21000 Dijon, France (e-mail: paul.walker@u-bourgogne.fr).

Alexandre Cochet is with the Laboratoire Imagerie et Vision Artificielle, EA 7535, University of Bourgogne-Franche-Comté, 21000 Dijon, France, also with the CHU François Mitterrand, 21000 Dijon, France, and also with the Georges-François Leclerc Cancer Centre, Unicancer, 21000 Dijon, France (e-mail: alexandre.cochet@cgfl.fr).

Jean-Marc Vrigneaud is with the Laboratoire Imagerie et Vision Artificielle, EA 7535, University of Bourgogne-Franche-Comté, 21000 Dijon, France, and also with the Georges-François Leclerc Cancer Centre, Unicancer, 21000 Dijon, France (e-mail: jmvrigneaud@cgfl.fr).

Color versions of one or more of the figures in this article are available online at <https://ieeexplore.ieee.org>.

Digital Object Identifier 10.1109/TMI.2020.3024722

thus paving the way to innovative *in vivo* applications. These systems often consisted of a microPET integrated into a clinical-size magnet [5], [16]. As a consequence, many of these prototypes do not fit the requirement of a preclinical environment. Indeed, setting-up PET/MR imaging remains challenging in many nuclear medicine preclinical laboratories where relatively large magnets are difficult to install, or in MR rooms where complying with the radiation protection regulations is often not straightforward.

The idea behind the present study was to set-up a fully integrated PET/MR scanner dedicated to rodents, with a compact design adapted to most preclinical laboratories. A 7 T magnetic field has been chosen to comply with the trend towards higher field observed in preclinical MRI. Therefore, a new compact integrated helium-free 7 T PET/MR scanner optimized for *in vivo* mouse and rat imaging was designed.

This new scanner has been designed from its conception to allow smooth operation of both techniques along with bed movement, anaesthesia, temperature control and optimal animal monitoring. One of the major challenges of such an integrated system is to minimize the mutual interferences between PET and MR instrumentations. Therefore, the present study aims at carefully assessing the performance characteristics of this new PET/MR system and mutual interference between PET and MR subsystems.

The PET subsystem was assessed complying with the NEMA NU-4-2008 standard [17]. Regarding the MR subsystem, to date, no performance assessment standard has been published for preclinical standalone or PET-coupled MR system. We implemented a procedure based on the American College of Radiology (ACR) recommendations for clinical MR scanners [18], which has already been quoted by other authors in the same research context [11], [12], [19]. A special focus was directed toward lesser studied parameters, although of importance for quantitative use of PET/MR, such as the image count versus radioactivity concentration relationship or the noise generated in magnetic resonance images by PET counting.

II. MATERIALS AND METHODS

A. Scanner Description

Experiments have been carried out on a fully integrated PET/MR prototype dedicated to mouse and rat imaging. A sequential version of this system including a 3 T magnet has been previously described [20]. Several design and instrumentation developments have been carried out to integrate the new PET subsystem inside the 7 T MR such as the installation of a new SiPM generation (SensL J-Series) and the integration of a copper bore shield between PET and MR subsystems. The electronics of the prototype were redesigned, with improved dead time from 850 ns (on the previous clip-on prototype) down to 204 ns. An overview of the system is displayed in Fig. 1. At the front of the system, a motorized support designed to reduce electromagnetic (EM) interferences allows accurate axial translations of the animal beds (Minerve, Esternay, France). The interchangeable beds include a mask

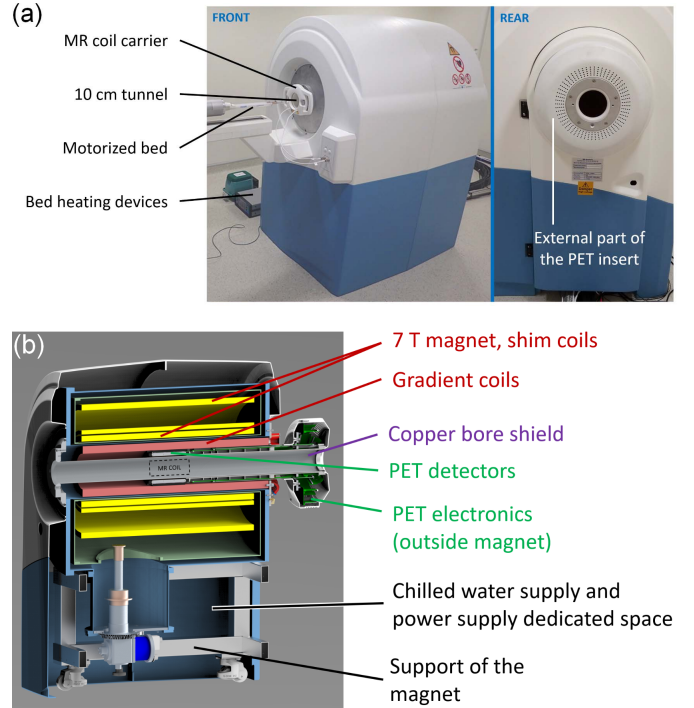


Fig. 1. External (a) and internal (b) overview of the integrated PET/MR system. The bed and the coil are inserted inside the PET detector.

TABLE I
PET CHARACTERISTICS

Detector modules	
Scintillators	LYSO
Crystal arrays	27 × 29, 28 × 30
Crystal dimensions	
External layer (mm × mm × mm)	1.605 × 1.605 × 6
Internal layer (mm × mm × mm)	1.605 × 1.605 × 4
Crystal pitch (mm)	1.68
SiPM series	SensL J-Series
SiPM arrays	12 × 12
SiPM tile size (mm × mm)	50.4 × 50.4
System	
Number of detector modules	16 (8 per ring, 2 rings)
Ring diameter (mm)	116
Transaxial FOV (mm)	80
Axial FOV (mm)	102.5
Coincidence time window (ns)	10
Energy window (keV)	250 - 750
Bore shield	
Composition	Axially extending copper stripes (two thicknesses)
Copper stripes thicknesses (μm)	35, 70

for the anaesthesia supply and a hot air circuit to maintain the animal's body temperature during examinations.

1) *PET Modality*: The annular PET subsystem is located between the RF coil and the MR bore as presented in Fig. 1b. A description of the PET subsystem is given in Table I. A diagram illustrating the PET detector's electronics is provided in Fig. 2. The PET subsystem contains sixteen detector heads arranged in two octagons of 116 mm in diameter. The axial FOV of the detector is 102.5 mm. A bespoke copper bore tube runs inside the PET, from the front to the back of the magnet, for EM shielding purpose. Two detector

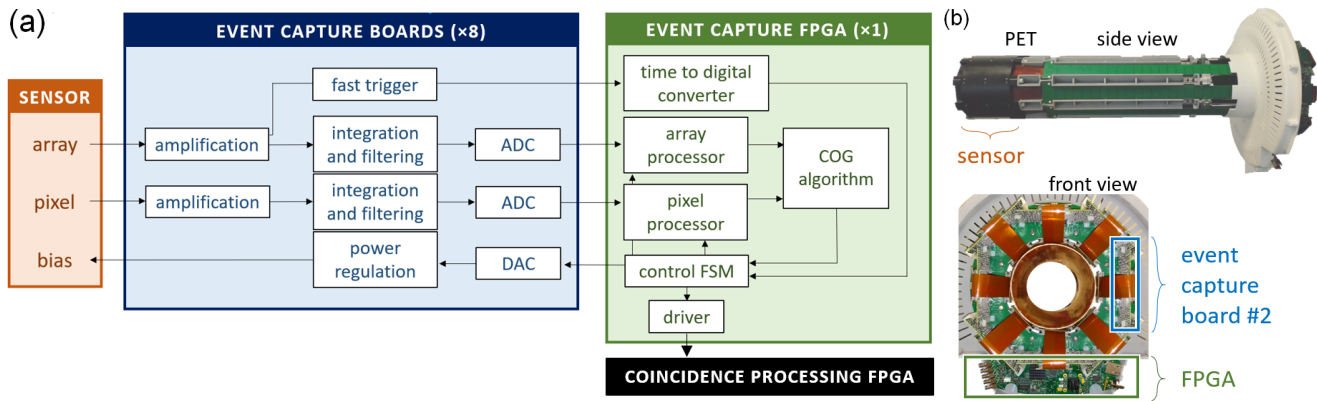


Fig. 2. (a) Diagram describing the PET electronics. ADC is for Analog-Digital Converter, DAC is for Digital-Analog Converter, COG is for Centre-Of-Gravity, and FSM is for Finite-State Machine. (b) Pictures of the PET subsystem removed from the MR bore and without its plastic shell. On the front view, one of the eight event capture boards and the FPGA board are highlighted.

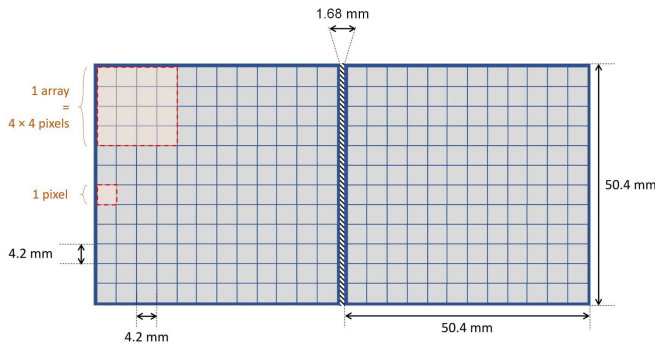


Fig. 3. Illustration of the SiPM tile structure. The two 50.4 mm side tiles are aligned in the axial direction forming a 102.5 mm axial field of view.

heads aligned in the axial direction are connected to a single sensor board. Each detector head contains a dual layer of cerium-doped lutetium yttrium oxyorthosilicate (Ce:LYSO) crystal arrays (EPIC Crystal Co Ltd, Jiangsu, China). The internal and external crystal arrays are respectively composed of 27×29 and 28×30 square pixels of 1.605 mm each side. Crystal thickness is respectively 6 mm and 4 mm for the external and internal layers. Alignment offset between the two crystal layers is half the pixel pitch, enabling depth of interaction (DOI) compensation. Each side of the individual pixels within the dual layer scintillator is coated with a $65 \mu\text{m}$ -width Vikuity™ enhanced specular reflector (ESR) (3M, St. Paul, MN, USA), and $10 \mu\text{m}$ of OP-20 adhesive (Dymax Europe GmbH, Wiesbaden, Germany), so that the total pixel pitch is 1.68 mm. A further ESR and a 1-mm thick K9 glass light guide (EPIC Crystal Co Ltd, Jiangsu, China) are present respectively on the top and at the bottom of the crystal array. The K9 glass is optically coupled to the crystal with $10 \mu\text{m}$ to $20 \mu\text{m}$ of BC-630 optical grease (Saint-Gobain, Courbevoie, France). In each detector head, the crystal matrix is coupled to a 12×12 SensL J-Series equally-spaced SiPM tile assembly (SensL, Cork, Ireland) (Fig. 3). The tile is multiplexed into 9 array-analog signals and 16 pixel-analog signals [21].

The two array- and pixel-analog signals from the SiPM are conducted out of the magnet thanks to long printed circuit board extensions. They are then filtered and amplified by the resistor–capacitor circuit in the event capture boards before being digitized by two 1,25 GHz ADCs, applying an integration time of respectively 70 ns and 90 ns for the array signal and the pixel signal. The fast array-signal is used for triggering purposes. It allows a fast and accurate timing information to be processed but a coarse positioning of the photon interaction. The slower pixel-signal gives more accurate energy and positional information. These signals are then passed through a field programmable gate array (FPGA) which calculates the X and Y positions of the interaction using Anger logic.

Each of the single photon events registered in the event capture boards is passed to a single controller board. The controller board processes the events into coincidences using timing and energy information from the array signal. A time walk correction (TWC) uses the energy of the event to correct for temporal variations in the trigger caused by difference in energy of the coincident events. After the application of the TWC, the digitized coincidence packet is sent to the acquisition processor via a 1 Gbit Ethernet cable. PET detectors trigger prompt counts if they are above the lower energy threshold and within a 10 ns coincidence time window. Random counts are collected in a delayed time window. The data sent via the 1 Gbit Ethernet is analyzed in real-time by the acquisition processor. This processor uses lookup tables to convert the Anger XY coordinates and raw energies into list-mode data (LMD), consisting of crystal positions and calibrated energies. A similar method has been described by [22].

The SensL J-series SiPMs [23] offer a linear relationship between temperature and gain. Temperature variations due to the gradient coil heating during certain MRI sequences are partially controlled by the gradient chiller. Further to this, the SiPM boards contain sixteen temperature sensors which feedback information to the software in order to control the SiPM bias. Since the gain of each SiPM depends on both the temperature and bias, it can be kept stable by an automatic update of the bias voltage.

Before reconstruction, the LMD is binned into prompt and random data structures, containing the module number, the crystal identification (ID) number (axial and transaxial positions, layer information) and the energy. The data can be reconstructed using either single slice rebinning (SSRB) [24] with 2D filtered backprojection (2D-FBP) or 3D ordered subsets expectation maximisation (3D-OSEM). For the FBP reconstruction, the prompt and random data structures are binned into sinograms by converting the crystal ID to a global coordinate within that crystal's boundaries. The number of bins is set to 81, with a bin width of 0.84 mm (half the crystal pitch) and 180 projection angles. In this work, a maximum ring difference of 8 was set during SSRB, meaning that an oblique line of response (LOR) can at most extend over 9 axial rings of crystals [25]. No arc-correction was applied. For the 3D-OSEM reconstruction, the LMD is binned into a structure compatible with the pre-calculated System Response Matrix (SRM). The data is sorted into coincidences of back to back modules and coincidences that are in non back to back modules. The SRM is specifically tailored to the detector geometry and makes use of transaxial/axial symmetries, mirror symmetries and rotation symmetries. The prompt and random data structures are filled accordingly after the detector response is normalized from a pre-determined detector lookup-table. The random data are then smoothed to produce a noiseless data set. The scatter fraction and its distribution are then calculated using an energy dependent scatter table [26] and the prompt data. The whole data set is then combined with the random data, to form a background data set. The background data set is used to correct the prompt data set during the reconstruction along as being corrected for decay and deadtime. Although an MR-based attenuation correction is available on the system, it was not used in the context of this study. The reconstruction software was provided by the PET manufacturer (*Preclinical Scan*, MR Solutions Ltd, Guildford, UK).

2) *MR Modality*: The microMR subsystem consists of a cryogen-free superconducting magnet [27] operating with a nominal magnetic flux density of 7 T (Flexiscan-MRS-7024-FL, MRS Magnetics Ltd, Guildford, UK). With the dry magnet technology, no helium supply is needed. The magnet has a length of 0.8 m and an outer diameter of 1.0 m. The 5-gauss line is located 1.2 m and 1.5 m from the magnet centre, respectively in the transaxial and axial planes. The room containing the MR scanner does not require a Faraday cage. The system is provided with mouse-sized and rat-sized quadrature coils ensuring both the transmission of the radiofrequency (RF) pulses and the reception of the nuclear magnetic resonance signal. Smaller RF coils are also available. A coil carrier enables coil switching. Table II provides a detailed description of the MR subsystem including the properties of the large rat body RF coil used for this work.

B. System Specifications

1) *PET NEMA Specifications and Linearity of Quantification*: This section deals with the PET performances. All the tests were carried out while the MR subsystem was idle (i.e. no sequence was pulsing).

TABLE II
MR SUBSYSTEM CHARACTERISTICS

Magnet	
Nominal magnetic flux density (T)	7
Diameter, length (m)	1.0, 0.8
Weight (kg)	600
Five-gauss line distance from centre (m)	1.2
Bore inner diameter (mm)	240
Elliptical FOV (mm × mm)	98 × 135
Gradient coil	
Gradients strength (X, Y, Z) (mT/m)	240
Maximal slew rate (X, Y, Z) (T/m/s)	1750, 1500, 1720
Internal/external diameter (mm)	160/227
RF coil	
Type	¹ H transmit-receive quadrature coil
Denomination	large rat body coil
Internal/external diameter (mm)	6.7/9.1
Position in the system	inside PET subsystem
Resonator length (mm)	64
Max. peak transmit power (kW)	2.0

a) *Spatial resolution*: The PET spatial resolution (SR) was assessed using a ²²Na point source (Eckert and Ziegler Isotopes Product, Valencia, USA) of 0.8 MBq at imaging time. The diameter of the subsystem and the presence of the coil did not allow us to measure the resolutions at the 25 mm radial position. The acquisitions were carried out at the following radial positions: 5 mm, 10 mm, 15 mm. An additional SR measurement was performed at the radial centre of the FOV. One-minute list-mode acquisitions were launched to collect more than 10⁵ prompt coincidences. One hundred and twenty three 2D sinograms containing 180 projections and 81 radial bins were produced by SSRB with a maximum ring difference of 8. Sinograms were then reconstructed with a 2D-FBP algorithm, with a voxel size of 0.28 mm × 0.28 mm × 0.42 mm. Random events were collected and stored for a dedicated correction. The full width at half maximum (FWHM) and the full width at tenth maximum (FWTM) were measured complying with the NEMA NU4-2008 standard [17] and were reported as the spatial resolution in the three axes.

b) *Sensitivity*: The ²²Na source described in the spatial resolution section was accurately positioned at the centre of the FOV (± 0.5 mm in all directions), and moved forward and backward by 0.84 mm steps in order to cover the entire axial FOV. A 1-minute acquisition was launched for every axial step. Acquisitions were also carried out without the rat large body coil previously mentioned in the MR subsystem description section. For practical reasons, only 19 source positions were tested for the *no coil* operation condition. A 1-minute background scan was also acquired. SSRB was then used to produce 2D sinograms (all ring differences allowed). An in-house program was used to calculate the absolute sensitivity of the system according to the NEMA NU4-2008 specifications [17]. Absolute sensitivity was also reported for every source location to build an axial sensitivity profile.

c) *Count rate*: A rat-like and a mouse-like phantom both complying with the NEMA-NU4-2008 standard [17] were filled with 70 MBq of fluorodeoxyglucose (¹⁸F-FDG) at the

acquisition start. Measurements and data processing were compliant with the NEMA NU4-2008 standard [17]. The acquisitions were carried out with and without the presence of a mouse-sized or rat-sized RF coil, depending on the NEMA phantom used. Intrinsic radiation of the detector was assessed with a twenty-four-hour background scan. The noise equivalent count rate (NECR) curves were calculated from the formula:

$$\text{NECR} = \frac{T^2}{T + S + R} \quad (1)$$

where T is the trues rate, R is the randoms rate and S is the rate of scatters.

d) Image quality: The NEMA NU-4-2008 [17] image quality (IQ) phantom was filled with a known activity of ^{18}F -FDG (3.7 MBq at acquisition time) and a 20 min list-mode acquisition over 1 bed position was launched. Data were reconstructed using 3D-OSEM with 2 iterations, 32 subsets, and a voxel size of 0.42 mm \times 0.42 mm \times 0.42 mm. Data were corrected for scatter, random, decay, normalization and dead time. Image analysis including recovery coefficients, spill over ratios (SOR) calculations on air and in water chambers, and standard deviations of SORs was carried out complying with the NEMA NU4-2008 standard [17].

e) Linearity of quantification: This test aimed at assessing the linearity of the image counts with activity. A 50 mL syringe was filled with a solution of ^{18}F -FDG. Twenty-three acquisitions were launched to cover an activity range from 50 MBq down to 0.1 MBq. The scans were all 30 min long, and were launched every hour. Data were reconstructed using 3D-OSEM (2 iterations, 32 subsets), a 0.56 mm isotropic voxel size and applying corrections for scatter, random, decay, normalization, and dead time. A cylindrical volume of interest (VOI) with a diameter of 13.4 mm and a length of 72.8 mm was traced. The mean voxel values in the VOI were reported as a function of the activity in the phantom.

2) MR Subsystem ACR Specifications: All acquisitions were carried out with the large rat quadrature coil. The phantom used for these tests was a 50 mL syringe, filled with a solution of physiological serum containing gadolinium at a concentration of 0.5 mmol/L. The phantom was centered in the MR FOV. The active shimming calibration was repeated before each acquisition.

a) Principal magnetic field homogeneity: This test was based on the phase difference map procedure described in detail in the ACR guide [18]. Coronal phase maps were obtained with a gradient echo sequence, with the following parameters: repetition time (TR) of 1000 ms, echo time (TE) of 3.14 and 7.62 ms, matrix of 128 \times 128 pixels, FOV of 60 mm \times 40 mm \times 4 mm, flip angle of 30°, 3 signal averages per acquisition. The test was performed in the central-coronal plane of a phantom mimicking a rat. The B_0 homogeneity was reported as the maximum minus minimum values of a circular region of 26.9 mm in diameter at the centre of the B_0 map.

b) B_1 homogeneity: A dual flip angle (FA) method based on Wang *et al.* [28] was set up. Two gradient echo images were acquired in the coronal plane, one with a flip angle of $\alpha = 45^\circ$,

the other with a FA of $2\alpha = 90^\circ$. The following parameters were employed: FOV of 60 mm \times 40 mm \times 4 mm, 3 signal averages per acquisition, TR of 1000 ms, TE of 5 ms, matrix 128 \times 128 pixels. A flip angle map α_{exp} , is calculated pixel by pixel with equation 2, where S_1 and S_2 represent the signals of low FA image and high FA image, respectively.

$$\alpha_{\text{exp}} = \cos^{-1} \left| \frac{S_2}{2 \times S_1} \right| \quad (2)$$

Signal mean \pm standard deviation (SD) was calculated on the FA map in a central circular region of 26.9 mm in diameter.

C. Mutual Interferences

1) Influence of MRI on PET: In this section, we present experiments concerning the stability of PET performance during MRI acquisitions. The influence of the MR subsystem on PET was assessed by running PET acquisitions with (pulsing operation condition) and without (idle operating condition) a simultaneous echo-planar imaging (EPI) sequence. The EPI sequence was chosen for its gradient-demanding aspect, which may cause more eddy currents than other sequences. The EPI sequence parameters were as followed: TR 2000 ms, TE 24 ms, flip angle of 90°, matrix of 64 \times 128, FOV of 40 mm \times 40 mm \times 4 mm, 14 signal averages.

a) Sensitivity: The sensitivity measurement described in the PET performance specifications was repeated with the EPI sequence pulsing. The profiles obtained with MR idle and MR pulsing were compared. For practical reasons, only 19 source positions were tested for the MR pulsing operation condition.

b) Energy resolution and coincidence time resolution: A one-minute scan of a point source was acquired in a rat body coil, with both operating conditions. Using this data, the energy resolution of each detector was calculated as the FWHM of the photopeak divided by the measured energy of the photopeak, expressed as a percentage. The energy resolution of the system was reported as the mean \pm SD for the sixteen PET modules of the dual-ring system. The coincidence time resolution (CTR) was reported as the FWHM of the coincidences timing histogram recorded by the direct opposite pairs of detectors. The histogram consisted in 31 bins of 0.8 ns. The energy resolution and the CTR obtained with and without MR pulsing were compared.

c) Count rate: List-mode acquisitions were performed with both phantoms (rat and mouse) during a simultaneous 24-hour long EPI acquisition. Count rates obtained with and without MR pulsing were compared.

d) Hot spot phantom: An ultra micro hot spot phantom with hollow channels having diameters of 0.7 mm, 0.8 mm, 0.9 mm, 1.0 mm, 1.1 mm, and 1.2 mm, was filled with 9 MBq of ^{18}F -FDG and imaged in list-mode during 30 minutes. Data were reconstructed using 3D-OSEM (1 to 10 iterations, 64 subsets) with a voxel size of 0.28 mm \times 0.28 mm \times 0.28 mm. The data were corrected for scatter, random, decay, normalization and dead time.

2) Influence of PET on MRI: All the measurements were carried out with the phantom described in the MR subsystem ACR performance section.

TABLE III

SUMMARY OF THE PET PERFORMANCE ASSESSMENT AND COMPATIBILITY STUDY PROTOCOL. THE FIRST COLUMN INDICATES THE POSITION OF THE TEST IN THE MATERIALS AND METHODS SECTION

Characteristic	MRI operating condition	MR coil	Radio-element	Activity (MBq)	Phantom	Scan duration (min)	Reconstruction algorithm	Voxel size (mm)	
PET Performance Evaluation									
B1a	Spatial resolution	idle	with	²² Na	0.8	n/a	1	2D-FBP	0.28 × 0.28 × 0.42
B1b	Sensitivity	idle	with, without	²² Na	0.8	n/a	1	n/a (SSRB)	n/a
B1c	Count rate	idle	with, without	¹⁸ F	70.0	rat-like, mouse-like	5 to 25	n/a (SSRB)	n/a
B1d	Image quality	idle	with	¹⁸ F	3.7	NEMA IQ	20	3D-OSEM	0.42 × 0.42 × 0.42
B1e	Quantification	idle	with	¹⁸ F	50.0	50 mL syringe	30	3D-OSEM	0.56 × 0.56 × 0.56
Influence of MRI on PET									
C1a	Sensitivity	idle, pulsing	with	²² Na	0.8	n/a	1	n/a (SSRB)	n/a
C1b	Energy resolution, CTR	idle, pulsing	with	²² Na	0.8	n/a	1	n/a	n/a
C1c	Count rate	idle, pulsing	with, without	¹⁸ F	70.0	rat-like, mouse-like	5 to 25	n/a (SSRB)	n/a
C1d	Hot spot phantom	idle, pulsing	with	¹⁸ F	9.0	ultra micro hot spot	30	3D-OSEM	0.28 × 0.28 × 0.28

TABLE IV

SUMMARY OF THE MR SUBSYSTEM PERFORMANCE ASSESSMENT AND COMPATIBILITY STUDY PROTOCOL. THE FIRST COLUMN INDICATES THE POSITION OF THE TEST IN THE MATERIALS AND METHODS SECTION. THE PHANTOM WAS A 50 mL SYRINGE FOR ALL THE MRI ASSESSMENT PROCEDURE

Characteristic	PET operating condition	Activity (MBq)	Sequence	TR (ms)	TE (ms)	matrix	FOV (mm × mm × mm)	FA (°)	Averages	
MRI Performance Evaluation										
B2a	B_0 homogeneity	idle	0	Gradient echo (2D)	1000	3.14, 7.62	128×128	60 × 60 × 4	30	3
B2b	B_1 homogeneity	idle	0	Gradient echo (2D)	1000	5	128×128	60 × 60 × 4	45, 90	3
Influence of PET on MRI										
C2a	B_0 homogeneity	idle, counting	82.0	Gradient echo (2D)	1000	3.14, 7.62	128×128	60 × 60 × 4	30	3
C2b	B_1 homogeneity	idle, counting	35.0	Gradient echo (2D)	1000	5	128×128	60 × 60 × 4	45, 90	3
C2c	Proton spectroscopy	idle, counting	97.0	PRESS (3D)	3000	26	n/a	$\begin{cases} 2 \times 2 \times 2 \\ 5 \times 5 \times 5 \\ 10 \times 10 \times 10 \end{cases}$	90	5
C2d	SNR	idle, counting	147.0	Spin echo (2D)	1000	20	256×256	60 × 60 × 2	90	3

a) *Principal magnetic field homogeneity*: The phantom was filled with a ¹⁸F-FDG solution containing an activity of 82 MBq at the MR acquisition start. The B_0 evaluation test previously described was performed while a PET acquisition was running.

b) *B_1 homogeneity*: The phantom was filled with a ¹⁸F-FDG solution containing an activity of 35 MBq at the MR acquisition start. In parallel with the B_0 homogeneity assessment procedure, the B_1 evaluation test previously described was performed while a PET acquisition was running.

c) *Proton spectroscopy*: Free induction decay curves were acquired using a point resolved spectroscopy sequence (PRESS) [29]. The PRESS sequence, allowing spatial encoding, was preferred to the One-Pulse sequence, as it would be more likely used for *in vivo* examination. The PRESS sequence was acquired with a 2.5 kHz spectral width. The sequence aimed at selecting three cube sizes localized at the centre of the phantom: 2 mm, 5 mm, and 10 mm. The acquisitions were carried out using a TR of 3000 ms, a TE of 26 ms, and five signal averages. A total of 4096 points were collected on the free induction decay (FID) curves to calculate the ¹H nuclear magnetic resonance (NMR) spectra by Fourier transform. FWHM of the proton resonance peaks were measured on the real part of each NMR spectra after

phase correction. For the PET active condition, the phantom was filled with 97 MBq.

d) *Signal-to-noise ratio of MR images*: Signal-to-noise ratio (SNR) was measured on spin echo images according to the ACR recommendations [18]. The phantom was injected with 147 MBq. One central slice of the phantom was acquired with a T1-weighted sequence using the following parameters: TR of 1000 ms, TE of 20 ms, matrix of 256 × 256, 3 signal averages, FOV of 60 mm × 60 mm × 2 mm. This acquisition was repeated nine times, in order to study an activity range going from 147 MBq to 7 MBq. SNR was calculated complying with the ACR recommendations and reported as a function of the activity in the phantom.

III. RESULTS

A. System Specifications

1) PET Specifications:

a) *Spatial resolution*: At the axial centre of the FOV, the radial FWHM/FWTM ranged from 1.74/3.32 mm at the centre of the FOV to 1.77/3.19 mm at a radial distance of 15 mm from the centre of the FOV. The tangential FWHM/FWTM ranged from 1.69/3.19 mm to 2.16/6.53 mm and the axial FWHM/FWTM ranged from 1.97/4.14 mm to 2.39/4.87 mm.

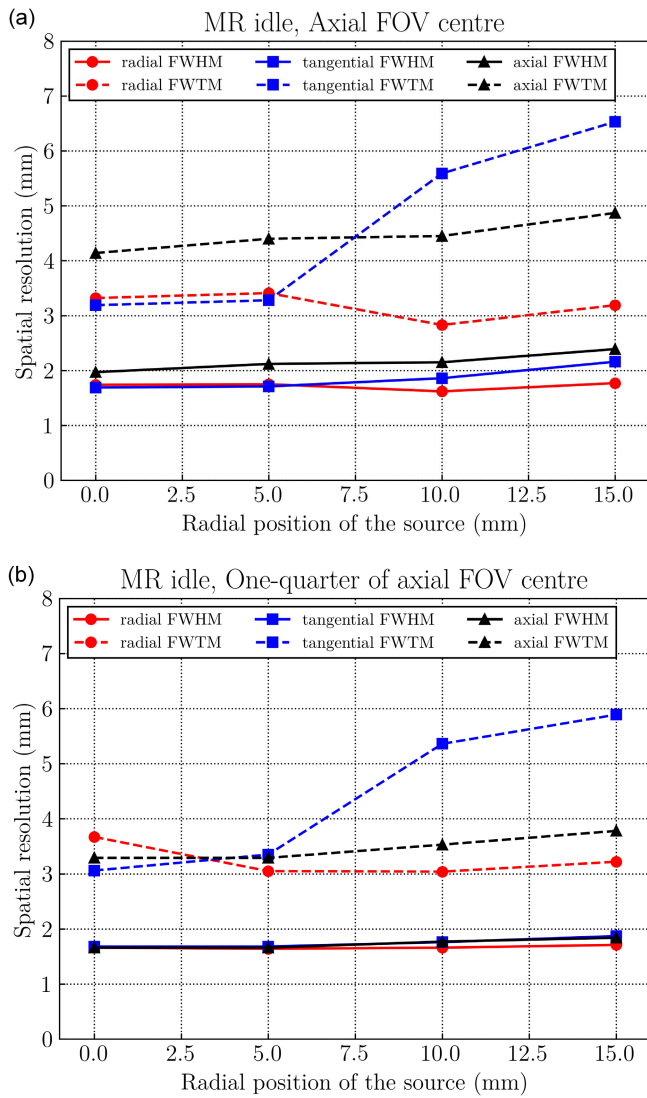


Fig. 4. PET spatial resolutions plotted against the axial position of the source, (a) at the FOV axial centre, and (b) at one quarter of the FOV axial centre. All measurements were done in MR idle operating condition, in the presence of the RF coil. Measurements and analysis were carried out complying with the NEMA-NU4-2008 standard [17].

Complementary measurements were performed at one quarter of the PET axial FOV to comply with the NEMA report [17]. Regarding these measurements, the radial FWHM/FWTM ranged from 1.66/3.67 mm at the radial centre of the FOV to 1.71/3.22 mm at a radial distance of 15 mm from the centre of the FOV. The tangential FWHM/FWTM ranged from 1.68/3.06 mm to 1.87/5.89 mm and the axial FWHM/FWTM ranged from 1.66/3.29 mm to 1.84/3.78 mm. The spatial resolutions are presented in Fig. 4 for every source location. Globally, FWHM values were not affected by the radial distance of the source. On the contrary, transverse FWTM values were quite unstable across the FOV, with a marked increase in tangential FWTM at the 10 and 15 mm radial positions. This effect is likely due to parallax errors in our octogon geometry and is explained in detail in the Discussion section. Besides, due to the presence of the gap between the two rings, the resolutions acquired at the PET axial FOV were

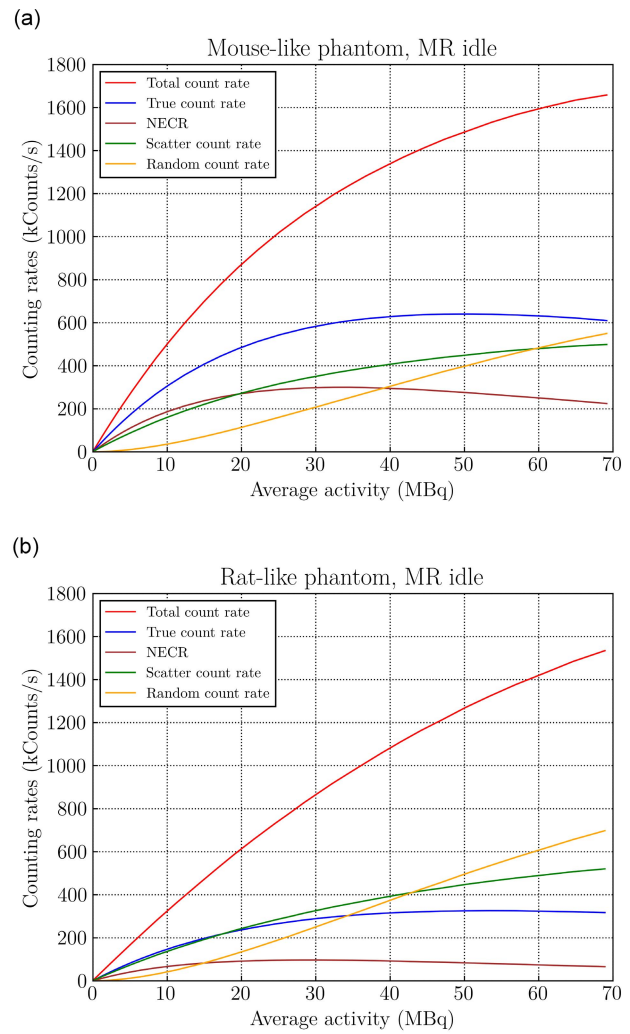


Fig. 5. Counting rates and NECR obtained in the presence of an RF coil, with the mouse-like phantom (a) and with the rat-like phantom (b). A 250–750 keV energy window was used.

slightly degraded compared to the resolutions acquired at one quarter of the PET axial FOV.

b) *Sensitivity*: Absolute system sensitivities were measured with an energy window of 250-750 keV. The peak sensitivity was 7.5% and 7.9% with and without a rat body coil installed in the MR subsystem, respectively. The system sensitivity axial profiles obtained with and without the MR coil are displayed in Fig. 8.

c) *Count rate*: With RF coil, the peak NECR obtained with respectively the mouse-like phantom and the rat-like phantom were 300.0 kcps at 34.5 MBq and 96.4 kcps at 30.2 MBq (Fig. 5). Without the presence of the coil, the peak NECR increased to 426.9 kcps at 34.3 MBq and 132.3 kcps at 28.4 MBq, respectively for the mouse and rat phantoms (Fig. 9).

d) *Image quality*: Uniformity and SOR parameters are presented in Table V. As a consequence of the absence of attenuation correction, the air chamber SOR was higher than the water chamber SOR. An overview of the NEMA-IQ images is displayed in Fig. 6.

TABLE V
NEMA-IQ PHANTOM RESULTS

	SOR	%SD
Air	25.3	14.2
Water	14.4	17.1
Rod diameter	Recovery coefficient (%)	
1 mm	25.1 ± 17.3	
2 mm	71.4 ± 13.3	
3 mm	90.4 ± 9.6	
4 mm	94.0 ± 9.6	
5 mm	95.9 ± 11.9	
Non uniformity (%)		5.7

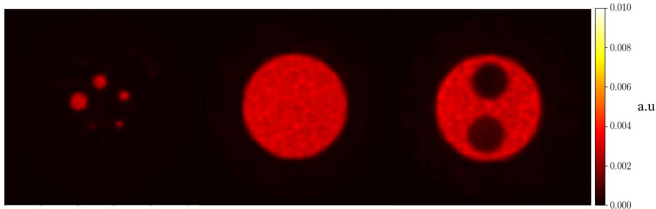


Fig. 6. Transverse slices of the three compartments of the NEMA-IQ phantom displayed with 0% to 100% of the maximum intensity pixel of the global image. Images were reconstructed in 3D-OSEM with 2 iterations, 32 subsets, 0.42 mm isotropic voxel size. Data were corrected for scatter, random, decay, normalization, and dead time.

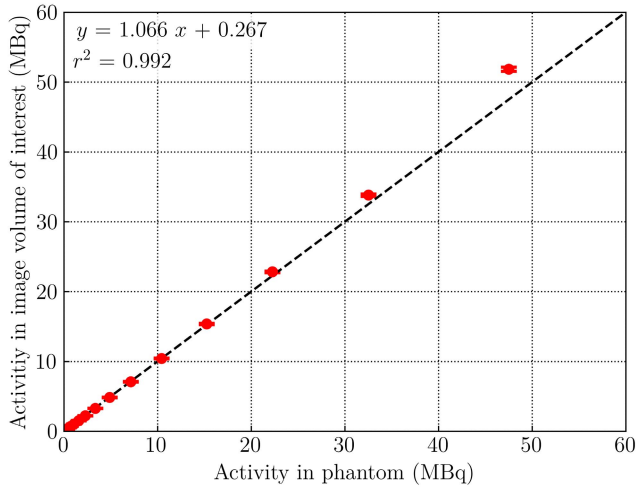


Fig. 7. Image counts plotted against the activity in the phantom. The black dotted line is the line of equality. Error bars are standard errors of the mean.

e) *Linearity of quantification:* The linearity of the radioactivity quantification was verified for activities up to 40 MBq. The linearity results are displayed in Fig. 7.

2) MR ACR specifications:

a) *Principal magnetic field homogeneity:* The B_0 variations ranged from -1.0 ppm to 0.5 ppm, in the coronal plane (Fig. 12a, left image).

b) B_1 homogeneity: In the coronal plane, the homogeneity of the pulse flip angle displayed as mean ± SD of FA in a 26.9 mm diameter circular region of interest was $46.1^\circ \pm 1.1^\circ$ with PET idle (Fig. 12b, left image). In the axial plane, in the same region, the homogeneity of FA was $43.0^\circ \pm 1.7^\circ$.

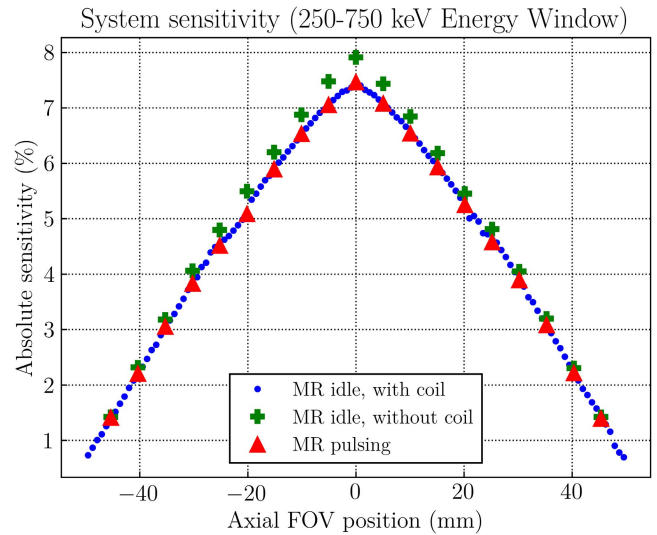


Fig. 8. Axial sensitivity profile in two different operating conditions (energy window = 250 – 750 keV).

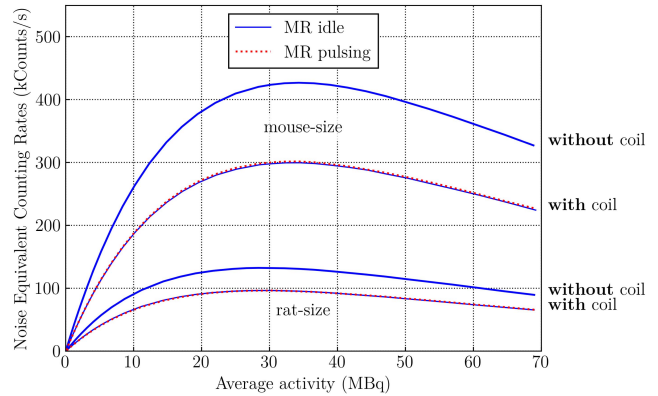


Fig. 9. NECR obtained with the rat-size and mouse-size NEMA phantoms, with and without the presence of an RF coil. Both operating conditions are displayed.

B. Mutual Interferences

1) Influence of MRI on PET:

a) *Sensitivity:* The peak absolute sensitivity of the system was 7.5% with and without MR pulsing. The axial profile of the absolute sensitivity is displayed for both operating conditions in Fig. 8. Negligible differences were observed between the two profiles, with no disruption of the curves.

b) *Energy resolution and coincidence time resolution:* The energy resolution of the system was found to be $20.9\% \pm 2.3\%$ with MR idle and $20.7\% \pm 2.2\%$ during MR pulsing. The CTR was 4.8 ± 0.5 ns with MR idle and 4.8 ± 0.4 ns with MR pulsing. CTR and energy resolutions are illustrated in Fig. 11.

c) *Count rate:* With MR pulsing, the peak NECR was 96.3 kecps at 30.3 MBq and 301.5 kecps at 34.3 MBq, respectively for the rat and mouse configurations. The relative change in the peak NECR between the two operating conditions, considering MR idle as a reference, was -0.1% and 0.5% for

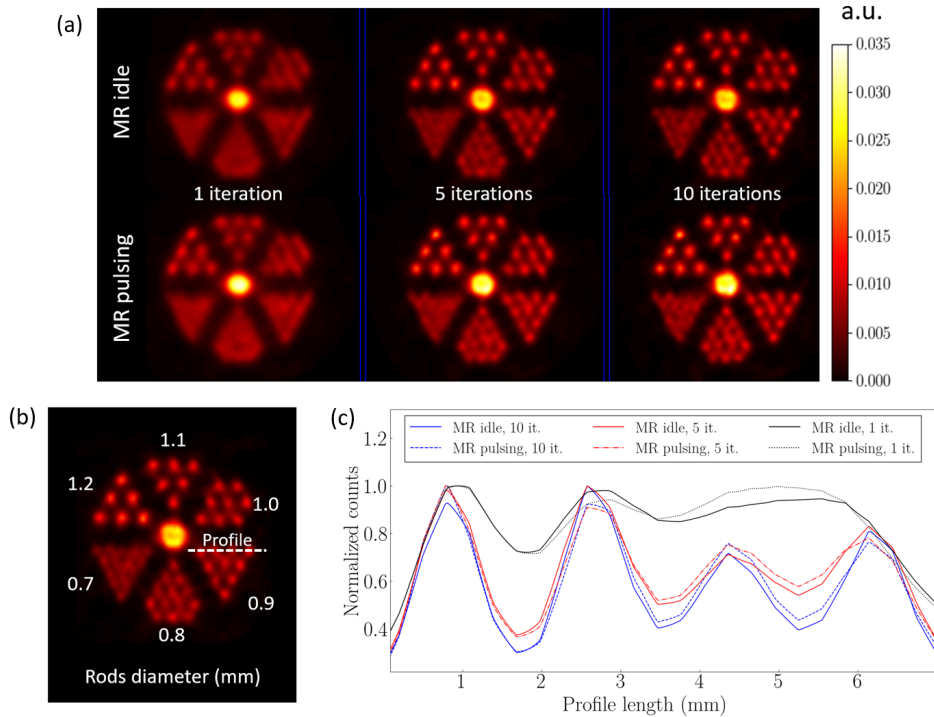


Fig. 10. (a) Transverse slices of the ultra micro hot spot phantom acquired with the MR idle (top line) and the MR pulsing (bottom line) operating conditions, with 1 iteration (left), 5 iterations (middle), and 10 iterations (right). (b) Illustration showing the rods diameter (in mm) and the position of the intensity profile (the white dotted line) on the 0.9 mm rods region. (c) The graph displays the normalized intensity profiles measured in the 1 iteration, 5 iterations, and 10 iterations reconstructed images.

the rat and mouse size of the phantom, respectively. A relative difference of about 30% was found between the peak NECR acquired with and without the presence of a MR coil. The NECR curves obtained with both sizes of phantom and with and without coil, are displayed in Fig. 9.

d) Hot spot phantom: We used a 3D-OSEM algorithm with 1 to 10 iterations and 64 subsets, a voxel size of $0.28 \text{ mm} \times 0.28 \text{ mm} \times 0.28 \text{ mm}$. Results were similar with both operating conditions. The rods with a diameter of 1.1 mm, 0.9 mm, and 0.8 mm were discernible with respectively one iteration, five iterations, and ten iterations as shown in Fig. 10.

2) Influence of PET on MRI:

a) Principal magnetic field homogeneity: Qualitatively, the B_0 maps obtained with PET available and PET active were similar, as shown in Fig. 12a. The B_0 variations ranged from -1.0 ppm to 0.5 ppm with PET available and from -1.0 ppm to 0.4 ppm with PET active.

b) B_1 homogeneity: In the coronal plane, the homogeneity of B_1 displayed as mean \pm SD of FA in a 26.9-mm diameter circular region of interest was $46.1^\circ \pm 1.1^\circ$ with PET available, and $45.7^\circ \pm 0.9^\circ$ with PET active. The PET available and the PET active flip angle maps are displayed in Fig. 12b. Quantitatively, 86% of the pixels of the coronal map were included between 40° and 50° , in both operating conditions.

c) Proton spectroscopy: FWHM of the resulting spectra were similar whether the PET was acquiring counts or not. Spectroscopy results are displayed in Table VI for both operating conditions.

d) Signal-to-noise of MR images: A decrease in SNR was observed in the spin echo images acquired simultaneously with

TABLE VI
PROTON SPECTROSCOPY RESULTS OBTAINED WITH THE PRESS SEQUENCE

Cube dimension:	FWHM (Hz)	
	PET idle	PET active
2 mm side	7.2 ± 0.1	7.7 ± 0.1
5 mm side	11.8 ± 0.6	12.8 ± 0.9
10 mm side	17.0 ± 0.6	15.6 ± 1.1

a PET image. This was observed for activities greater than 20 MBq. The evolution of the spin echo image SNR as a function of the radioactivity in the phantom is presented in Fig. 13.

IV. DISCUSSION

A. PET Performance

One noteworthy feature of this integrated prototype in comparison with other systems, is the peak system sensitivity almost reaching 8% (Table VII). This is explainable by the high solid angle of detection of the PET system, provided by its internal diameter of 11.6 cm and axial FOV of 10 cm.

The FBP volumetric resolution (VR) of the system, defined as the product of the FWHM in the three orthogonal directions, reached 5.8 mm^3 at the centre of the axial FOV. This result is slightly higher than VR at FOV quarter in comparison to other integrated scanners (Table VII). As noted by [30], the use of FBP, as required by NEMA, can be inadequate with some specific geometries and can lead to broad artefacts. To overcome this problem, some authors have implemented

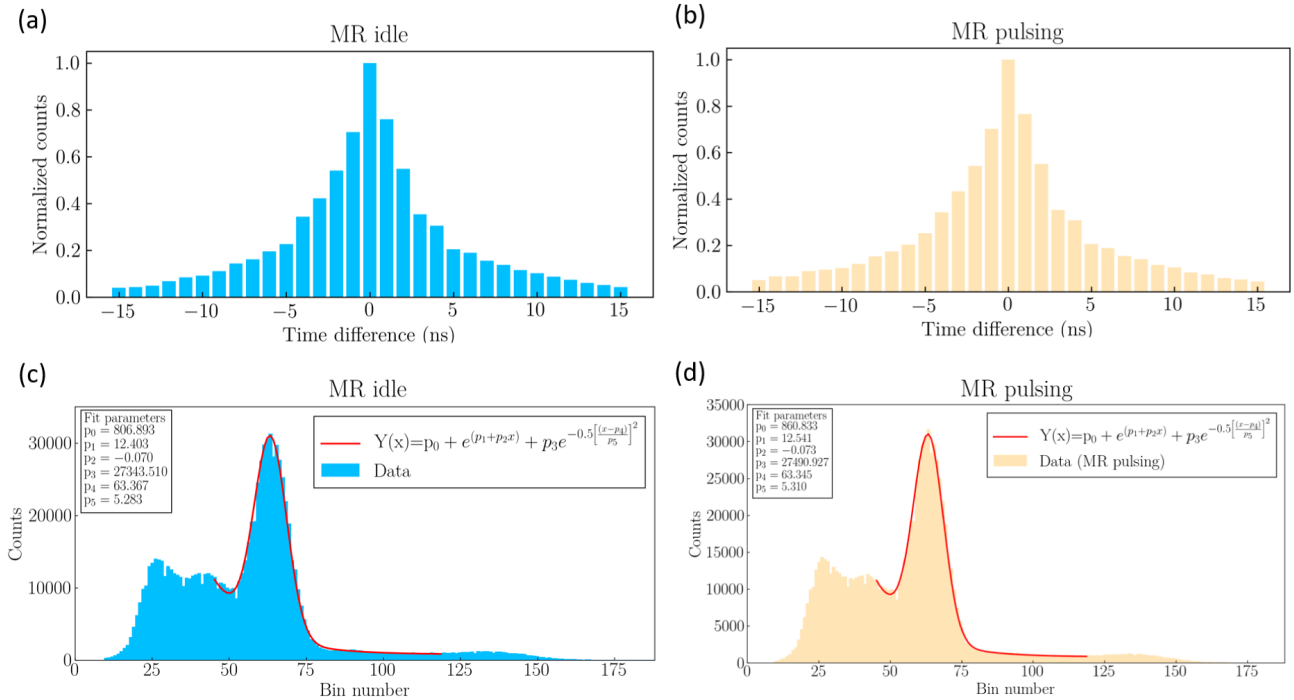


Fig. 11. Timing histograms obtained for one detector using respectively the MR idle (a) and MR pulsing (b) operating conditions. Energy histograms obtained for one detector using respectively the MR idle (c) and MR pulsing (d) operating conditions.

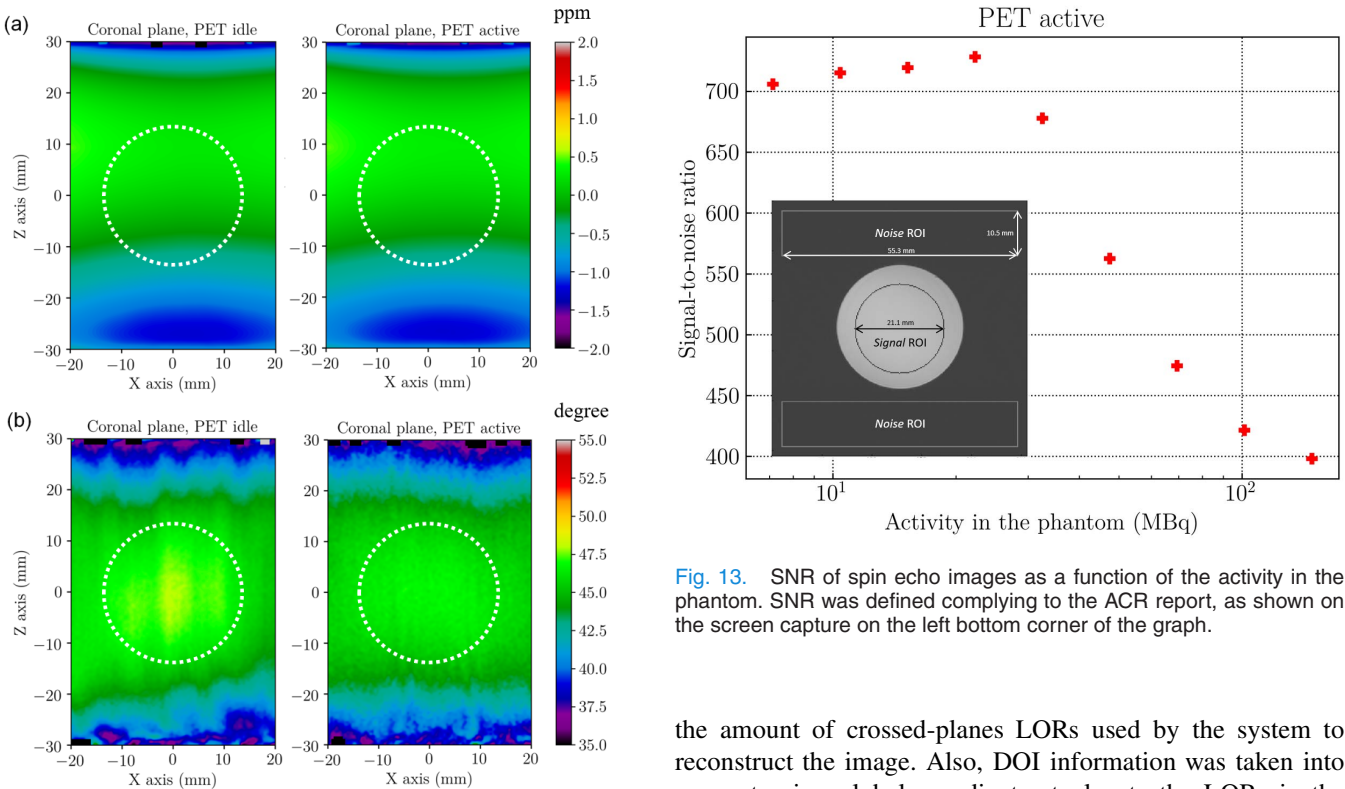


Fig. 12. (a) Principal magnetic field distortion map in ppm of B_0 field. (b) Flip angle maps, expressed in degrees. The expected flip angle is 45° . B_0 and B_1 are displayed for the two PET operating conditions. The white dotted lines indicate the analysed ROI boundaries.

strategies to deal with the histogramming of data to be used with FBP, trying to preserve DOI information [31]. We chose to reduce the maximum ring difference in SSRB to limit

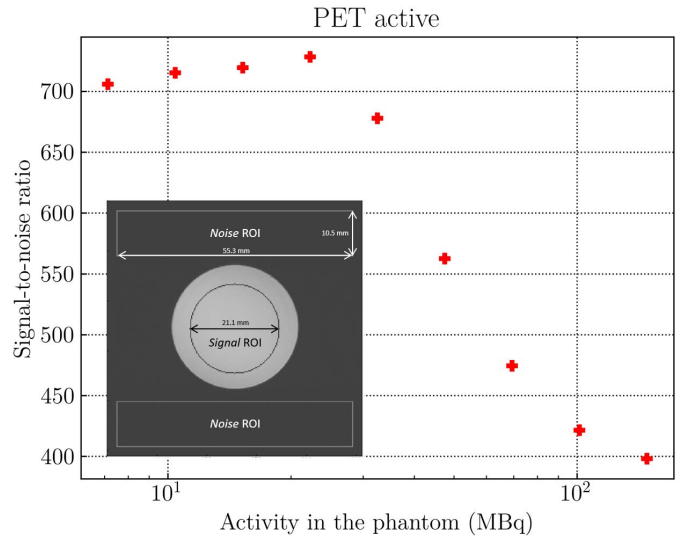


Fig. 13. SNR of spin echo images as a function of the activity in the phantom. SNR was defined complying to the ACR report, as shown on the screen capture on the left bottom corner of the graph.

the amount of crossed-planes LORs used by the system to reconstruct the image. Also, DOI information was taken into account using global coordinates to locate the LORs in the sinograms. However, transverse FWTM values were still found to be degraded at some offset positions due to a star-like artefact, with lines of excess activity a bit more pronounced in the tangential direction. The artefact shares similarities with those observed with other scanner geometries composed of a limited number of detector heads to form the ring [10], [32]. Moreover, resolutions measured at the axial FOV centre were

TABLE VII
SUMMARY OF THE PROTOTYPE SPECIFICATIONS AND COMPARISON WITH OTHER SMALL ANIMAL INTEGRATED PET/MR SYSTEMS

Systems	Large magnets			Compact dry magnets	
	MADPET4	Stortz <i>et al.</i>	HYPERION-II	SimPET	This study
Related articles	[5], [6]	[13]–[15]	[10]–[12]	[7], [8], [9]	
Compatible rodent size	mouse, rat	mouse	mouse, rat, rabbit	mouse	mouse, rat
MRI					
Magnetic flux density (T)	7	7	3	7, 1 [†]	7
Clear bore size (mm)	300	200	600	200, 126 [‡]	240
RF coil internal diameter (mm)	31, 150	35	46, 160	35, 30 [‡]	65
B_0 distortion (ppm) / FOV (mm × mm) *	0.4 / (20 × 40)	0.3 / (35 × 70)	2.0 / (30 × 60)	0.4 / (35 × 60)	1.5 / (40 × 60)
PET					
Energy window (keV)	250 [§]	300-800	250-625	250-750	250-750
Internal ring diameter (mm)	88	60	210	64, 60 [‡]	116
Axial FOV (mm)	20	28	97	55, 50 [‡]	103
Temperature variation compensation	no	yes	yes	yes	yes
DOI effects compensation	yes	yes	no	no	yes
Radial SR at FOV centre (mm)	1.29	1.17	n/a	1.31	1.74
Tangential SR at FOV centre (mm)	1.29	1.35	n/a	1.14	1.69
FBP Volumetric SR at FOV centre (mm ³)	2.7	2.1	4.9	1.9	5.8
FBP Volumetric SR at FOV quarter (mm ³)	2.9	2.1	4.9	7.3	4.6
Maximum sensitivity (%)	0.7	2.2	4.0	3.4, 4.2 [‡]	7.5, 7.9 [†]
Mouse NECR peak (kcps)	29	21	407	42, 151 [‡]	300, 427 [†]
Mouse NECR peak (MBq)	103	15	46	15, 38 [‡]	35, 34 [†]
Mouse scatter fraction (%)	19	15	13	17, 22 [‡]	34, 24 [†]
Rat NECR peak (kcps)	n/a	n/a	n/a	n/a	96, 132 [†]
Rat NECR peak (MBq)	n/a	n/a	n/a	n/a	30, 28 [†]
Rat scatter fraction (%)	n/a	n/a	n/a	n/a	48, 41 [†]

*Approximated from the B_0 maps found in the related article. [†]Measured in the absence of the RF coil.

[‡]Energy threshold (time-over-threshold method). [‡]Instrumental update of the SimPET, integrated in a 1-T permanent magnet.

slightly degraded by the presence of the axial inter ring gap of 1.68 mm and 3.36 mm respectively for the external and internal crystal layers. None of the above artefacts were identified with OSEM and, since the preclinical data are usually reconstructed using an iterative method like OSEM, the NEMA results might not reflect the *in vivo* performance of the system. For example, the 0.8 mm rods of the phantom were discernible on the ultra micro hot spot phantom with ten iterations (Fig. 10).

The drawback of an axial assembly in comparison with a continuous sensor is the presence of an interdetector area where no photons can be detected. One frequent consequence of this is the disruptive aspect of the sensitivity profiles ([5], [10]). However, only a slight perturbation of the sensitivity profile was observed on this system (Fig. 8). The loss of LOR caused by this central gap is insignificant relative to the total number of LORs collected in the FOV.

The NECR measurements revealed the ability of this system to deal with high counting rates, as summarized in Table VII. This can be explained by both instrumentation and electronics improvements. Indeed, the last generation J-Series SiPMs (SensL, Cork, Ireland), offering a high photon detection efficiency [33], was here combined with a FPGA firmware optimized for high count rate acquisitions. All our measurements, including the NECR acquisitions, have been performed by a real-time recording of the coincidence position and the photon energy, instead of a full raw capture board readout transfer to the capture PC acquisition processor. The count rate improvement brought by this method has been previously suggested by Hallen *et al.* [10]. The linearity of

the image count versus activity was verified on this system up to 40 MBq.

The attenuation and scattering of gamma rays in the RF coil caused a roughly 5% decrease in peak sensitivity, and 30% decrease in peak NECR in both rat and mouse configurations. This highlights the opportunity of further sensitivity and counting rate improvements by modification of the coil design.

B. MR Subsystem Performance

Regarding MR performance, the main concerns are the homogeneity of B_0 and B_1 and the SNR. These characteristics might be degraded by the integration of the PET subsystem in the MR bore, and during simultaneous scans. Moreover, B_0 heterogeneity can cause image distortions, inaccurate fat suppression, and SNR decrease [18]. B_0 homogeneity measurements were based on the phase difference map presented in the ACR guide. With this procedure, the phase difference between the two acquired phase maps is affected only by the field heterogeneity, which increases the accuracy of the result compared with other tests [18]. This test was thereby chosen by many authors for the B_0 homogeneity evaluation [6], [8], [15], [16]. This test is not strictly speaking a standardized method. As explained in the ACR report, it aims at being adapted individually by users for a longitudinal follow up. Nevertheless, it allows an approximate inter-system comparison. The homogeneity of the principal magnetic field was evaluated in the central-coronal plane of a phantom mimicking a rat. The results of the tests were in accordance with the manufacturer's specifications for the standalone magnet.

At the centre of the FOV, a variation of about 0.03 ppm/mm was observed regardless of the operating conditions. The homogeneity of the principal magnetic field is similar to that reported in other studies (Table VII).

Qualitatively, the B_1 distortions were found on the boundaries of the FOV, as expected. This was observed in other prototypes [6], [15].

C. PET/MR Interferences

During the conception of the system, particular attention was paid to the reduction of EM interferences between both modalities. In particular, the PET was designed to move the PET electronics out of the MR bore as much as possible. A bespoke copper cylinder was also included between the RF coil and the PET detectors. The choice of this RF shield material was a trade-off between several factors [34] such as skin depth and linear attenuation coefficient, in order to optimise the RF shielding without causing too much attenuation for the annihilation photons. The high scatter fractions measured on the PET detector (Table VII) might be due to the plastic material of the MR coil. Indeed, as shown in Table VII, the system scatter fraction of 34% obtained with the mouse phantom in the presence of the MR coil is reduced down to 24% when the coil is removed.

Regarding the influence of MRI on PET, the sensitivity, the energy resolution, the CTR, and the NECR, were found to be equivalent with and without MR pulsing. We were not able to compare these data with other systems, due to the lack of related literature. Like Weissler *et al.* [11], we did not notice any distortion of the image of the ultra micro hot spot phantom when the MR subsystem was pulsing. All these results demonstrated the EM immunity of the PET instrumentation and electronics with respect to the static magnetic field and RF, thanks to the design of the system (electronics located outside the magnet, EM shielding) and thanks to the ability of the PET to compensate for the gradient-induced temperature variation of the SiPM.

Regarding the influence of PET on MRI, B_0 and B_1 maps were similar with and without PET counting, thereby proving the absence of influence of the PET activity on the RF homogeneity. This is similar to the results obtained on the MADPET4 [6]. One notable result of the present study was the SNR decrease in spin echo images when the PET was counting. This was also described by Omidvari *et al.* [6] and Weissler *et al.* [11]. We furthermore observed that the SNR decrease, caused by an increase of the background noise, was strongly dependent on the amount of radioactivity in the phantom. This effect was only perceivable when the phantom was filled with an activity greater than 20 MBq, and when the PET was acquiring counts. The SNR fully recovered without any latency and regardless of the activity, after the PET acquisition. These results suggest that there is a detectable residual radio frequency interference between the PET electronics and the MR RF coil and bore shield.

V. CONCLUSION

This article presents the design and performance of a new simultaneous PET/MR preclinical prototype. The system

allows the acquisition of a rodent whole body image in a single step. It relies on a dual octagonal assembly of sixteen SiPM PET detectors fully integrated in the bore of a compact 7 T dry magnet. A bore shield prevents EM interferences. The bias voltage of the SiPM is adjusted in real-time to compensate for the temperature variations of the PET detector. The PET subsystem is highly sensitive and allows high count rates acquisitions. Indeed, the peak absolute sensitivity is 7.5%, and the peak NECR is 96.4 kcps at 30.2 MBq and 132.3 kcps at 28.4 MBq respectively for the rat-like and mouse-like NEMA count rate phantoms. The radioactivity is accurately quantified up to 40 MBq. At high activity, MR images suffer from an SNR decrease in proportion to the activity in the FOV. Regarding MRI, the magnetic field homogeneity meets what is observed with a standalone magnet. Moreover, no major modification of the PET and MR performance was observed during simultaneous imaging.

ACKNOWLEDGMENT

The authors would like to thank the following persons for their contribution. The team of the Nuclear Medicine Department of the Georges-François Leclerc Cancer Centre. B. Collin and A. Oudot from the CGFL preclinical facility. W. Scott-Jackson, G. Balmer, A. Camacho, F. Chaumard, J. Brown, C. Cirel, T. Becker, and D. Taylor from MR-Solutions Ltd.

REFERENCES

- [1] C. S. Levin, S. H. Maramraju, M. M. Khalighi, T. W. Deller, G. Delso, and F. Jansen, "Design features and mutual compatibility studies of the Time-of-Flight PET capable GE SIGNA PET/MR system," *IEEE Trans. Med. Imag.*, vol. 35, no. 8, pp. 1907–1914, Aug. 2016. [Online]. Available: <http://ieeexplore.ieee.org/document/7429780/>
- [2] B. J. Pichler, H. F. Wehrl, A. Kolb, and M. S. Judenhofer, "Positron emission Tomography/Magnetic resonance imaging: The next generation of multimodality imaging?" *Seminars Nucl. Med.*, vol. 38, no. 3, pp. 199–208, May 2008. [Online]. Available: <http://linkinghub.elsevier.com/retrieve/pii/S000129980800024X>
- [3] T. Y. Song, H. Wu, S. Komarov, S. B. Siegel, and Y.-C. Tai, "A sub-millimeter resolution PET detector module using a multi-pixel photon counter array," *Phys. Med. Biol.*, vol. 55, no. 9, pp. 2573–2587, May 2010. [Online]. Available: <http://stacks.iop.org/0031-9155/55/i=9/a=010?key=crossref.e60772c695c55%76cb2935574c60ad27d>
- [4] A. J. Gonzalez *et al.*, "A PET design based on SiPM and monolithic LYSO crystals: Performance evaluation," *IEEE Trans. Nucl. Sci.*, vol. 63, no. 5, pp. 2471–2477, Oct. 2016. <http://ieeexplore.ieee.org/document/7494679/>
- [5] N. Omidvari *et al.*, "PET performance evaluation of MADPET4: A small animal PET insert for a 7 t MRI scanner," *Phys. Med. Biol.*, vol. 62, no. 22, pp. 8671–8692, Nov. 2017. [Online]. Available: <http://iopscience.iop.org/article/10.1088/1361-6560/aa910d>
- [6] N. Omidvari, G. Topping, J. Cabello, S. Paul, M. Schwaiger, and S. I. Ziegler, "MR-compatibility assessment of MADPET4: A study of interferences between an SiPM-based PET insert and a 7 t MRI system," *Phys. Med. Biol.*, vol. 63, no. 9, May 2018, Art. no. 095002. [Online]. Available: <http://stacks.iop.org/0031-9155/63/i=9/a=095002?key=crossref.51e538e145%7d92a840e3697fa9d083a4>
- [7] G. B. Ko *et al.*, "Evaluation of a silicon photomultiplier PET insert for simultaneous PET and MR imaging: Silicon photomultiplier PET insert for simultaneous PET/MRI," *Med. Phys.*, vol. 43, no. 1, pp. 72–83, Dec. 2015, doi: [10.1118/1.4937784](https://doi.org/10.1118/1.4937784).
- [8] G. B. Ko *et al.*, "Simultaneous multiparametric PET/MRI with silicon photomultiplier PET and ultra-high-field MRI for small-animal imaging," *J Nucl Med.*, vol. 57, no. 8, pp. 1309–1315, Aug. 2016. [Online]. Available: <http://jnm.snmjournals.org/cgi/doi/10.2967/jnumed.115.170019>

- [9] J.-W. Son *et al.*, "SimPET: A preclinical PET insert for simultaneous PET/MR imaging," *Mol. Imag. Biol.*, vol. 22, no. 5, pp. 1208–1217, Apr. 2020. [Online]. Available: <http://link.springer.com/10.1007/s11307-020-01491-y>
- [10] P. Hallen *et al.*, "PET performance evaluation of the small-animal hyperion II d PET/MRI insert based on the NEMA NU-4 standard," *Biomed. Phys. Eng. Exp.*, vol. 4, no. 6, Oct. 2018, Art. no. 065027. [Online]. Available: <http://stacks.iop.org/2057-1976/4/i=6/a=065027?key=crossref.dce37ba0dce%633b235d5c17229d824ab>
- [11] B. Weissler *et al.*, "MR compatibility aspects of a silicon photomultiplier-based PET/RF insert with integrated digitisation," *Phys. Med. Biol.*, vol. 59, no. 17, pp. 5119–5139, Sep. 2014. [Online]. Available: <http://stacks.iop.org/0031-9155/59/i=17/a=5119?key=crossref.faf698467e5f%875e05e9eb0e29d0d460a>
- [12] B. Weissler *et al.*, "A digital preclinical PET/MRI insert and initial results," *IEEE Trans. Med. Imag.*, vol. 34, no. 11, pp. 2258–2270, Nov. 2015. [Online]. Available: <http://ieeexplore.ieee.org/document/7097723/>
- [13] G. Stortz *et al.*, "Performance of a PET insert for high-resolution small-animal PET/MRI at 7 tesla," *J. Nucl. Med.*, vol. 59, no. 3, pp. 536–542, Mar. 2018. [Online]. Available: <http://jnm.snmjournals.org/lookup/doi/10.2967/jnumed.116.187666>
- [14] A. L. Goertzen *et al.*, "First results from a high-resolution small animal SiPM PET insert for PET/MR imaging at 7T," *IEEE Trans. Nucl. Sci.*, vol. 63, no. 5, pp. 2424–2433, Oct. 2016. <http://ieeexplore.ieee.org/document/7485872/>
- [15] J. D. Thiessen *et al.*, "MR-compatibility of a high-resolution small animal PET insert operating inside a 7 T MRI," *Phys. Med. Biol.*, vol. 61, no. 22, pp. 7934–7956, Nov. 2016. [Online]. Available: <http://stacks.iop.org/0031-9155/61/i=22/a=7934?key=crossref.a15f5fba93d%660ad4c3483dde0091cda>
- [16] J. Wehner *et al.*, "MR-compatibility assessment of the first preclinical PET-MRI insert equipped with digital silicon photomultipliers," *Phys. Med. Biol.*, vol. 60, no. 6, pp. 2231–2255, Mar. 2015. [Online]. Available: <http://stacks.iop.org/0031-9155/60/i=6/a=2231?key=crossref.c3351a1ebf17%e41dc0696273a3095812>
- [17] *Performance measurements of small animal positron emission tomographs*, National Electrical Manufacturers Association, Rosslyn, AN, USA, 2008.
- [18] *2015 Magnetic resonance imaging quality control manual*, Amer. College Radiol., Reston, VA, USA, Oct. 2015.
- [19] P. M. Däppenbecker *et al.*, "Development of an MRI-compatible digital SiPM detector stack for simultaneous PET/MRI," *Biomed. Phys. Eng. Exp.*, vol. 2, no. 1, Feb. 2016, Art. no. 015010. [Online]. Available: <http://stacks.iop.org/2057-1976/2/i=1/a=015010?key=crossref.dbcd1637920%309720d553e685916f2>
- [20] J. M. Vrigneaud *et al.*, "Initial performance evaluation of a preclinical PET scanner available as a clip-on assembly in a sequential PET/MRI system," *Phys. Med. Biol.*, vol. 63, no. 12, Jun. 2018, Art. no. 125007. [Online]. Available: <http://stacks.iop.org/0031-9155/63/i=12/a=125007?key=crossref.086b1d494%097fe53e3d6e5ac25b9355>
- [21] (2012). *Matrix Readout System for Nuclear Medicine Detection*. [Online]. Available: <http://www.sensl.com/downloads/ds/UM-MatrixSM9.pdf>
- [22] C.-Y. Liu and A. L. Goertzen, "Improved event positioning in a gamma ray detector using an iterative position-weighted centre-of-gravity algorithm," *Phys. Med. Biol.*, vol. 58, no. 14, pp. N189–N200, Jul. 2013. [Online]. Available: <http://stacks.iop.org/0031-9155/58/i=14/a=N189?key=crossref.63bc4b7ac05%2987398d186af29430554>
- [23] J. Du, X. Bai, and S. R. Cherry, "Performance comparison of depth-encoding detectors based on dual-ended readout and different SiPMs for high-resolution PET applications," *Phys. Med. & Biol.*, vol. 64, no. 15, p. 15NT03, Aug. 2019. [Online]. Available: <https://iopscience.iop.org/article/10.1088/1361-6560/ab1c37>
- [24] M. E. Daube-Witherspoon and G. Muehllehner, "Treatment of axial data in three-dimensional PET," *J. Nucl. Med.*, vol. 28, no. 11, pp. 1717–1724, 1987.
- [25] F. H. Fahey, "Data Acquisition in PET Imaging," *J. Nucl. Med. Technol.*, vol. 30, no. 2, p. 12, 2002.
- [26] H.-T. Chen, C.-M. Kao, B. C. Penney, and C.-T. Chen, "Evaluation of an energy-based method for scatter correction in positron emission tomography," in *Proc. IEEE Nucl. Sci. Symp. Conf. Rec.*, San Diego, CA, USA, Dec. 2006, pp. 3297–3304. [Online]. Available: <http://ieeexplore.ieee.org/document/4179754/>
- [27] R. A. Ackermann, K. G. Herd, and W. E. Chen, "Advanced Cryocooler Cooling for MRI Systems," in *Cryocoolers*, R. G. Ross, Ed. Boston, MA, USA: Kluwer, 2002, pp. 857–867. [Online]. Available: http://link.springer.com/10.1007/0-306-47090-X_101
- [28] J. Wang, W. Mao, M. Qiu, M. B. Smith, and R. T. Constable, "Factors influencing flip angle mapping in MRI: RF pulse shape, slice-select gradients, off-resonance excitation, and B0 inhomogeneities," *Magn. Reson. Med.*, vol. 56, no. 2, pp. 463–468, Aug. 2006. [Online]. Available: <http://doi.wiley.com/10.1002/mrm.20947>
- [29] U. Klose, "Measurement sequences for single voxel proton MR spectroscopy," *Eur. J. Radiol.*, vol. 67, no. 2, pp. 194–201, Aug. 2008. [Online]. Available: <https://linkinghub.elsevier.com/retrieve/pii/S0720048X08001897>
- [30] P. Hallen, D. Schug, and V. Schulz, "Comments on the NEMA NU 4-2008 standard on performance measurement of small animal positron emission tomographs," *EJNMMI Phys.*, vol. 7, no. 1, pp. 1–20, Dec. 2020. [Online]. Available: <https://ejnmiphys.springeropen.com/articles/10.1186/s40658-020-0279-2>
- [31] G. Stortz *et al.*, "Characterization of a new MR compatible small animal PET scanner using monte-carlo simulations," *IEEE Trans. Nucl. Sci.*, vol. 60, no. 3, pp. 1637–1644, Jun. 2013. [Online]. Available: <http://ieeexplore.ieee.org/document/6515698/>
- [32] A. Etxebeste *et al.*, "Study of sensitivity and resolution for full ring PET prototypes based on continuous crystals and analytical modeling of the light distribution," *Phys. Med. Biol.*, vol. 64, no. 3, Jan. 2019, Art. no. 035015. [Online]. Available: <https://iopscience.iop.org/article/10.1088/1361-6560/aaf7ba>
- [33] M. Amirrashedi *et al.*, "NEMA NU-4 2008 performance evaluation of Xtrim-PET: A prototype SiPM-based preclinical scanner," *Med Phys.*, vol. 46, no. 11, pp. 4816–4825, Aug. 2019. [Online]. Available: <https://onlinelibrary.wiley.com/doi/abs/10.1002/mp.13785>
- [34] P. M. Duppenbecker *et al.*, "Gradient transparent RF housing for simultaneous PET/MRI using carbon fiber composites," in *Proc. Nuclear Sci. Symp. Med. Imag. Conf. (NSS/MIC)*, Anaheim, CA, USA, Oct. 2012, pp. 3478–3480. [Online]. Available: <http://ieeexplore.ieee.org/document/6551793/>